Proceedings of the ASME 2020 15th International Manufacturing Science and Engineering Conference
MSEC2020
June 22-26, 2020, Cincinnati, OH, USA

MSEC2020-8339

LASER-INDUCED NANOCARBON FORMATION FOR TUNING SURFACE PROPERTIES OF COMMERCIAL POLYMERS

Moataz Abdulhafez
Department of Industrial Engineering
University of Pittsburgh, Pittsburgh, PA, USA

Angela J. McComb
Department of Industrial Engineering
University of Pittsburgh, Pittsburgh, PA, USA

Mostafa Bedewy*
Department of Industrial Engineering
Department of Chemical and Petroleum Engineering
Department of Mechanical Engineering and Materials Science
University of Pittsburgh, Pittsburgh, PA, USA
*mbedewy@pitt.edu

ABSTRACT

The growth of laser-induced nanocarbons, referred to here are LINC for short, directly on polymeric surfaces is a promising route toward surface engineering of commercial polymers. This paper aims to demonstrate how this new approach can enable achieving varied surface properties based on tuning the nanostructured morphology of the formed graphitic material on commercial polyimide (Kapton) films. We elucidate the effects of tuning laser processing parameters on the achieved nanoscale morphology and the resulting surface hydrophobicity or hydrophilicity. Our results show that by varying lasing power, rastering speed, laser spot size, and line-to-line gap sizes, a wide range of water contact angles are possible, i.e. from below 20° to above 110°. Combining water contact angle measurements from an optical tensiometer with LINC surface characterization using optical microscopy, electron microscopy, and Raman spectroscopy enables building the process-structure-property relationship. Our findings reveal that both the value of contact angle and the anisotropic wetting behavior of LINC on polyimide are dependent on their hierarchical surface nanostructure which ranges for isotropic nanoporous morphology to fibrous morphology. Results also show that increasing gap sizes lead to an increase in contact angles and thus an increase in the hydrophobicity of the surface. Hence, our work highlight the potential of this approach for manufacturing flexible devices with tailored surfaces.

1. INTRODUCTION

Although the applications of commodity polymers are ubiquitous, controlling their surface properties in a scalable and affordable process is still challenging. This is particularly important for emerging applications of flexible device manufacturing. Recently, it has been shown that nanoscale graphitic structures can be synthesized by directly lasing of polyimide, a popular polymer, with commercially available low-cost infrared (IR) lasers [1]. The resulting material has been described in literature as: laser-induced porous graphene [1], laser induced graphene [2–4], laser-induced hierarchical carbon [5], or simply graphitic carbon [6]. Here, we use the term laser induced nanocarbon (LINC) to describe the material, which is a more representative term for to the diversity of the generated nanoscale carbon material types formed by this process, which include fibers and sheets [7]. These LINC structures have been shown to exhibit excellent electrical and thermal conductivities as well as high surface area. In addition, different morphologies have been observed at the microscale for LINC materials, ranging from porous to fibrous [7]. Accordingly, wide-reaching potential applications of LINC such as anti-fouling [8], anti-icing [9] and antimicrobial [10] surfaces have been investigated.

Recent research has also shown that LINC surface properties depend on lasing parameters such as laser power and speed [4,11,12]. Lamberti et al. [11] has shown that by changing the laser speed and power, different morphologies of polyimide-based LINC lines can be achieved. The different line morphologies, described as sheets, needles and porous had superhydrophobic contact angles. Tiliakos et al. [12] modulated laser power, scan rate, and step interval at a fixed laser spot size to control the morphology of 1 cm^2 LINC areas. Their results have shown that LINC areas range from superhydrophobic to

hydrophilic. They explain their results using topographical observations on the samples like hierarchical structures that combine macroscale and microscale roughness leading to superhydrophobic results and porous structures leading to hydrophilic results. Nevertheless, no anisotropy of contact angle was observed in that study. Additionally, Li et al. [4] have shown that by changing the lasing environment using a gas-controlled chamber, the contact angle between water droplets and LINC areas can be switched between superhydrophobic (>150°) and superhydrophilic by tuning the oxygen content in different gas atmospheres.

In this paper, we demonstrate the capability of tuning the anisotropic contact angles of LINC formed directly on the surfaces of the commercial polyimide films (Kapton) by lasing in air. We explore the effect of different laser processing parameters including laser power, speed, spot size, and rastering line-to-line gaps on water contact angle measured in two orthogonal directions. As a result, we are able to tune the surface properties in a large range of contact angles ranging from below 20° to above 110°. Importantly, this tunability can be achieved by only changing the lasing rastering parameters in atmospheric conditions (i.e. in air environment), which greatly simplifies the process since no special controlled-gas chamber is needed. Moreover, we propose a mechanism to explain the observed difference in contact angle measurements at different parameters by correlating contact angle with scanning electron microscopy (SEM) observations of the LINC areas.

2. METHODS

2.1. Sample preparation

The experiment was conducted by laser scribing on polyimide (PI) tape, also referred to as Kapton, (Grainger, Cat. No. 15C616, thickness: 3.5 mil), which was applied to a glass slide with a rubber roller to eliminate air bubbles. The glass slide maintains the flatness of the polyimide film during lasing. Prior to lasing, the polyimide surface is chemically cleaned by rinsing with acetone, followed by rinsing with isopropyl and quickly drying using a compressed air gun.

2.2. LINC Processing

A commercial CO_2 laser system (Full Spectrum Laser Pro-Series 20x12, 1.5 inch focus lens) with 10.6 μm wavelength and 45W laser power, was used for all lasing experiments. The system allows tuning the power by controlling the laser current. The beam diameter ($2w_x$) based on ($1/e^2$) was measured to be 220 μm. The laser objective lens is mounted on an XYZ stage with a maximum rastering speed of 500 mm/s.

2.3. Experiment design

As shown in Figure 1a, each slide has 4 square patches (1.27 cm × 1.27 cm) that are lased at different conditions. A single LINC patch is formed by laser rastering that proceeds as following: lasing in the positive x-direction a distance (L) at speed v, then shifting by an increment (g) in the y-direction, followed by lasing in the negative x-direction by the same distance (L) (Fig. 1b). This sequence is repeated until the square is completed. The laser machine input design file is generated by programming a MATLAB script with lines and a certain number of pixels gap between lines representing a single patch.

Experiments in this study were carried out by varying laser powers (P) between 12W and 28W, speed (v) between 350 mm/s and 500 mm/s, and the line-to-line gap (g) between 0 pixels, and 7 pixels (with increments of 3), where one pixel represents a shift of 50.8 μm (Fig. 1). Finally, the patches were rotated 90° for a total of two orientations in order to investigate contact angle anisotropy (Fig. 1b). The complete lasing and measurements parameters used in this study are presented in Table 1.

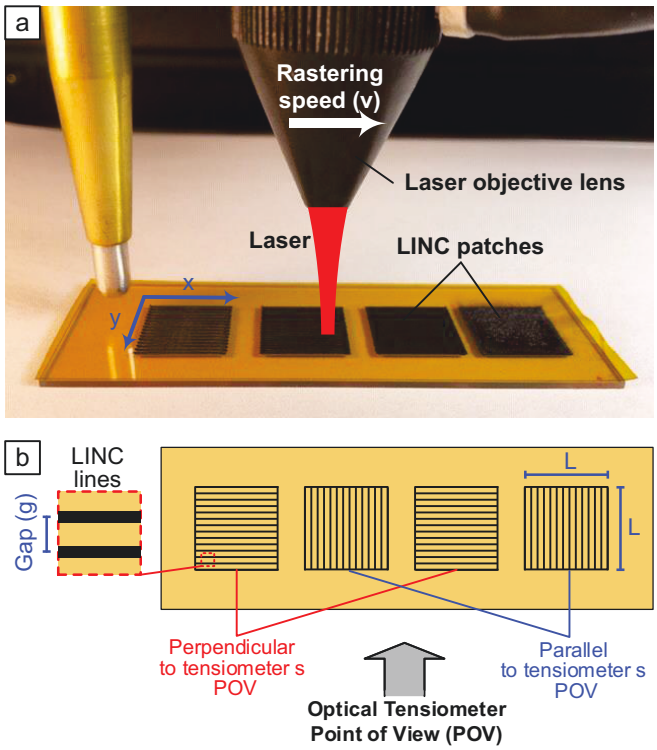

Figure 1: (a) Photograph of the setup showing both the laser objective lens and the sample of polyimide tape on glass with four LINC patches one it. (b) Schematic of each polyimide-covered glass slide with LINC patches at different orientations of rastering.

Table 1: Laser parameters used in this study

Parameter	Values
Speed (v) [mm/s]	500, 310
Power [W]	12, 28
Gap (g) [μm]	50.8, 203.2, 304.8, 406.4
Spot size radius (w_y) [μm]	100, 300
Orientation of optical tensiometer measurements relative to rastering direction	Perpendicular, Parallel

2.4. Contact angle (CA) measurements

Quantitative results were obtained by measuring the Young-Laplace's contact angle using a Biolin Scientific Optical Tensiometer. The process included ejecting four 5 µl water droplets on each sample and recording the results at ≈ 7 frames per second for 20 seconds. Afterwards, the software OneAttention was used to analyze each droplet by fitting the contact angle (CA) of the droplet for each of the 140 frames. The average of the 140 contact angles was then recorded as the contact angle for each measured droplet. Four drops are used for each condition on the same patch and the average and standard deviation of the contact angle are recorded.

2.4. Morphology characterization

To characterize the morphology of the LINC patches, scanning electron microscopy (SEM) images were taken with a Zeiss SIGMA VP Scanning Electron Microscope. Moreover, carbon structure was also characterized by Raman spectroscopy measurements (Xplora, Horiba Scientific) using the 638 nm excitation wavelength.

3. RESULTS

Before lasing of the polyimide samples, the CA of water on the native surface was measured, in order to be used as a control measurement for this study. Water CA on polyimide was measured to have an average of 88°. The experimental study is divided into 8 cases, each with different parameters as listed in Table 1. First, we are demonstrate the capability of our approach to generate patterns of LINC on flexible polyimide films, as depicted in Figure 2a. Figure 2b shows the Raman spectrum collected from one of the laser patches, exhibiting the characteristic G, D and 2D peaks associated with sp^2 carbon, which confirms the formation of high quality graphitic carbon.

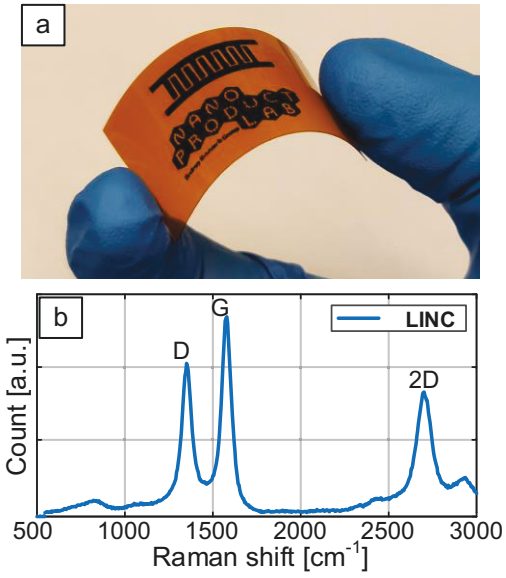

Figure 2: (a) Image illustrating direct writing of LINC on flexible substrates. (b) Raman spectra of LINC sample.

3.1. Case 1 (P = 28W, v = 500 mm/s, w_y = 300 µm)

Figure 3 illustrates the results at lasing power of 28 W, rastering speed of 500 mm/s and laser spot size of 300 µm. The g = 50.8 µm case exhibits a grey color with no visible periodicity in the patch, the color of the patch gets darker with increasing gap up to g = 304.8 µm. At g = 406.4 µm the line patterns are visible but the color is not as dark. At g = 50.8 µm, the contact angle measured in the perpendicular and parallel directions are very low at around 20°. With increasing gap, the angle increases to be higher than the control value, with the value in the parallel direction being higher than the perpendicular direction until it drops for both directions at g = 406.4 µm. At that point, the average perpendicular contact angle drop to around 20°, while the parallel contact angle drops slightly lower than the control. Hence, the patch with 406.4 µm gap exhibits the most CA anisotropy.

3.2. Case 2 (P = 28W, v = 350 mm/s, w_y = 300 µm)

Figure 4 illustrates the results at lasing power of 28W, rastering speed of 350 mm/s and laser spot size of 300 µm. These are the same parameters of Case 1, except at a lower speed indicating higher fluence delivered to the polyimide during lasing. The g = 50.8 µm also exhibits a grey color with no visible periodicity in the patch, the color of the patch gets darker up to a maximum at g = 304.8 µm. At g = 304.8 µm and g = 406.4 µm, the line patterns are visible but the patch color are not very dark. At g = 50.8 µm, the contact angle is maximum at around 100°. The contact angle displays a decreasing pattern similar the largest gap in Case 1 with the lowest contact angle in the perpendicular direction at around 50°. Again at g = 406.4 µm, the drop anisotropy is highest.

3.3. Case 3 (P =12W, v = 500 mm/s, w_y = 300 µm)

Figure 5 illustrates the results at lasing power of 12W, rastering speed of 500 mm/s and laser spot size of 300 µm. These are the same parameters of Case 1, except at a lower power indicating lower fluence delivered to the polyimide surface during lasing. From the image, none of the patches exhibit any change in color indicating very limited, if any, carbonization of polyimide. The contact angles show little change from the control value of bare polyimide, However, with increasing gap, drop anisotropy is noted to increase, illustrating the effect of surface patterning of anisotropy, even for low fluence cases.

3.4. Case 4 (P = 12W, v = 350 mm/s, w_y = 300 µm)

Figure 6 illustrates the results at lasing power of 12W, lasing speed of 350 mm/s and laser spot size of 300 µm. These are the same parameters of Case 2, except at a lower power indicating less fluence delivered when lasing. The g = 50.8 µm is the darkest patch, the color of the patch gets lighter till a minimum at g = 406.4 µm, indicating less carbonization at these gap values The line pattern is noticed in all patches. Drop anisotropy is highest at g = 406.4 µm. The patches are noticeably hydrophilic at g = 203.2 µm with contact angles between 15-20°, in contrast with the other patches, which show values closer to the control.

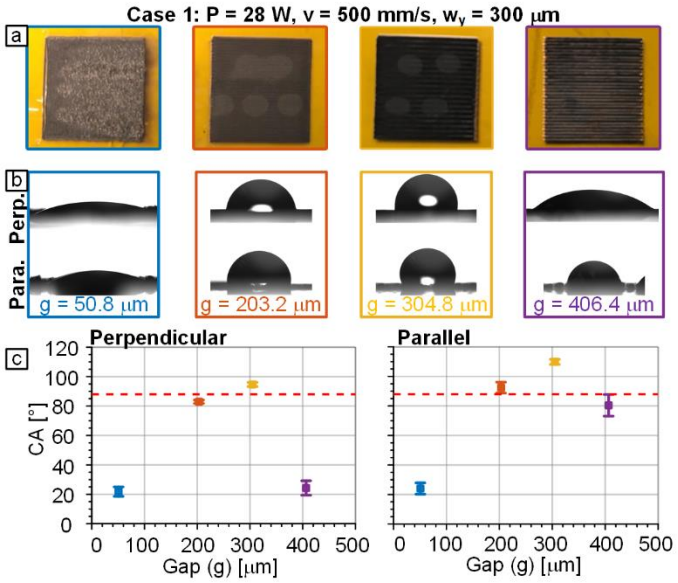

Figure 3: (a) Top view image of each patch for case 1 (lasing parameters P = 28W, v = 500 mm/s, w_y = 300 μm). (b) Optical tensiometer images of water droplets. (c) Plots of contact (CA) at different gap values. Red line represents control CA. Error bars represent ±standard deviation.

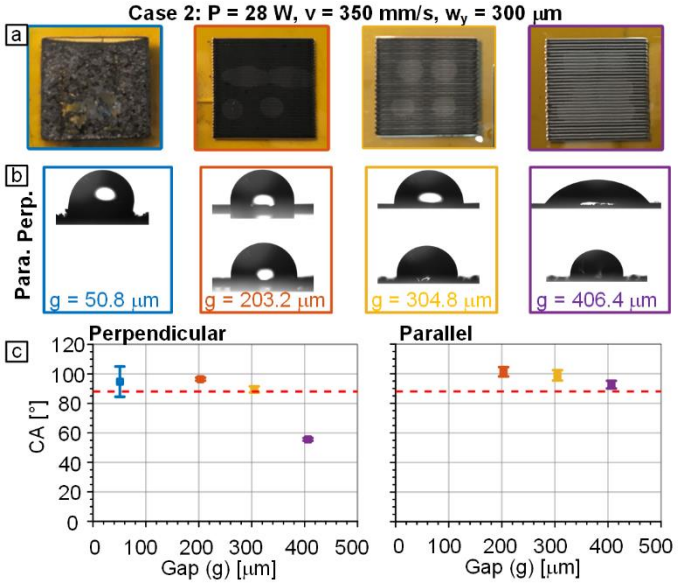

Figure 4: (a) Top view image of each patch for case 2 (lasing parameters P = 28W, v = 350 mm/s, w_y = 300 μm). (b) Optical tensiometer images of water droplets. (c) Plots of contact (CA) at different gap values. Red line represents control CA. Error bars represent ±standard deviation.

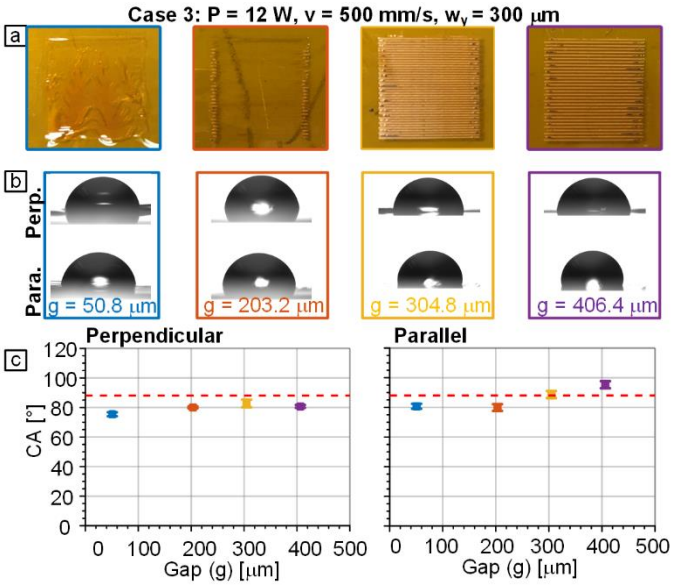

Figure 5: (a) Top view image of each patch for case 3 (lasing parameters P =12W, v = 500 mm/s, w_y = 300 μm). (b) Optical tensiometer images of water droplets. (c) Plots of contact (CA) at different gap values. Red line represents control CA. Error bars represent ±standard deviation.

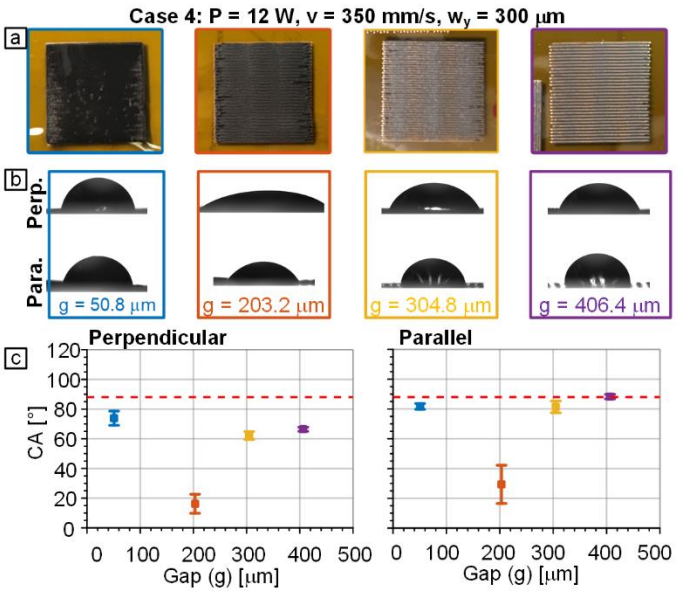

Figure 6: (a) Top view image of each patch for case 4 (lasing parameters P = 12W, v = 350 mm/s, w_y = 300 μm). (b) Optical tensiometer images of water droplets. (c) Plots of contact (CA) at different gap values. Red line represents control CA. Error bars represent ±standard deviation.

3.5. Case 5 (P = 28W, v = 500 mm/s, w_y = 100 μm)

Figure 7 illustrates the results at lasing power of 28W, rastering speed of 500 mm/s and laser spot size of 100 μm. These parameters are the same as Case 1, except that it has a smaller spot size. The g = 50.8 μm case exhibits a grey color, at g = 203.2 μm, the color is darker. At higher gaps the line patters are more visible, but the lines themselves are very dark. At g = 50.8 μm, the contact angle in the perpendicular and parallel direction are relatively low (in the range of 40-60°), with increasing gap, the angle increases to be around the control value. The perpendicular contact angle drops at g = 304.8 μm to increase again at g = 406.4 μm.

3.6. Case 6 (P = 28W, v = 350 mm/s, w_y = 100 μm)

Figure 8 illustrates the results at lasing power of 28W, rastering speed of 350 mm/s and laser spot size of 100 μm. These are the same parameters of Case 5, except at a lower speed indicating higher fluence delivered to the polyimide surface during lasing. All patches exhibit a very dark color, representing the darkest case of all 8 cases. At g = 50.8 μm, the droplets immediately wick: they are drawn into the patches through capillary action. At higher gaps, the drops have an increasing contact angle that is maximum around 115° parallel with 75° perpendicular.

3.7. Case 7 (P = 12W, v = 500 mm/s, w_y = 100 μm)

Figure 9 illustrates the results at lasing power of 28W, rastering speed of 350 mm/s and laser spot size of 100 μm. These are the same parameters of Case 5, except at a lower power indicating lower fluence delivered to the polyimide surface during lasing. The patches with the smallest two gaps have a darker color while the larger two gaps have a lighter color (closer to the original color of Kapton), indicating less carbonization. The patches are initially hydrophilic at g = 50.8 μm and g = 203.2 μm. At higher gaps, the contact angles measured from a parallel view to the lasing lines is hydrophic at a maximum of 100°, with the perpendicular contact angle at 50°, exhibiting contact angle anisotropy.

3.8. Case 8 (P = 28W, v = 350 mm/s, w_y = 100 μm)

Figure 10 illustrates the results at lasing power of 28W, rasterting speed of 350 mm/s and laser spot size of 100 μm. These are the same parameters of Case 6, except at a lower power indicating lower fluence delivered to the polyimide surface during lasing. Similar to case 7, The patches with the smaller two gaps have a darker color while the larger two gaps have a lighter color (closer to the original color of Kapton), indicating less carbonization. However, the patches at g = 304.8 μm and g = 406.4 μm exhibit alternating light and dark patterns along the lines, that repeat with each line. Like case 7, the contact angle changes from isotropic hydrophilic to hydrophobic at a maximum parallel contact angle at around 105° with maximum anisotropy observed at g = 406.4 μm.

4. DISCUSSION

To explain the observed difference in contact angle measurements and their dependence on lasing conditions, we correlate the observed behavior with the morphology of the patches as seen in SEM images. We imaged LINC lines formed with lasing power of 28W and rastering speed of 500 mm/s. We focused our measurements on two gaps: g = 50.8 μm and g = 203.2 μm, as shown in Figure 11. It is evident from the differences between the two cases that gap size plays an important role in morphology.

At g = 50.8 μm, high overlap between lased lines (Fig. 11 c, e) is observed, whereas g = 203.2 μm shows less overlap (Fig.11 d, f). Since the spacing between the laser paths at g = 50.8 μm is small compared to the spot size diameter of 200 μm, where each point on the area along the lased line would have been lased for around 4 passes. When the g = 203.2 μm, the overlap is minimized since the line-to-line distance is almost equal to the spot size. From the SEM imaging, the high overlap in g = 50.8 μm resulted in a porous morphology, looking much like a sponge (Fig. 11 g, i). This enhances water wicking through the internal porosity owing to the capillary effects. Hence, this nanoporous morphology leads to lower contact angles (~53°). On the other hand, the sample with g = 203.2 μm that has less overlap, exhibited a larger contact angle (~100°) and a more fibrous morphology (Fig. 11 h, j). This suggests that the high overlap between the lased lines led to the destruction of formed fibers, hence the nanoporous morphology. The high contact angle noted with the fiber formations implies that fibrous LINC formations lead to hydrophobic drop behavior.

We summarize the results of the different cases in Table 2. We also color code the results according the hydrophobicity or hydrophilicity of the surface (according to the measured water contact angle). Taken together, our results show that a number of interacting factors contribute to the observed value and anisotropy of water contact angle on LINC patches.

Water contact angle on LINC depends on the extent of carbonization of the polyimide surface, the resulting topography of the surface, and the internal porous morphology. These surface properties in turn result from laser processing parameters: lasing power, rastering speed, spot size, and how much overlap there is between rastering lines. Understanding these complex process-structure-property relationships is key for achieving a high degree of tunability of both the values and anisotropy of water contact angle. As observed in Table 2, the parallel orientation generally has a higher contact angles as compared to its perpendicular counterparts due to the directional topographic effects that causes pinning of water droplets at LINC lines leading to anisotropic drop shapes. In general, it is observed that the contact angles shift to hydrophobic progressively with increasing gap size.

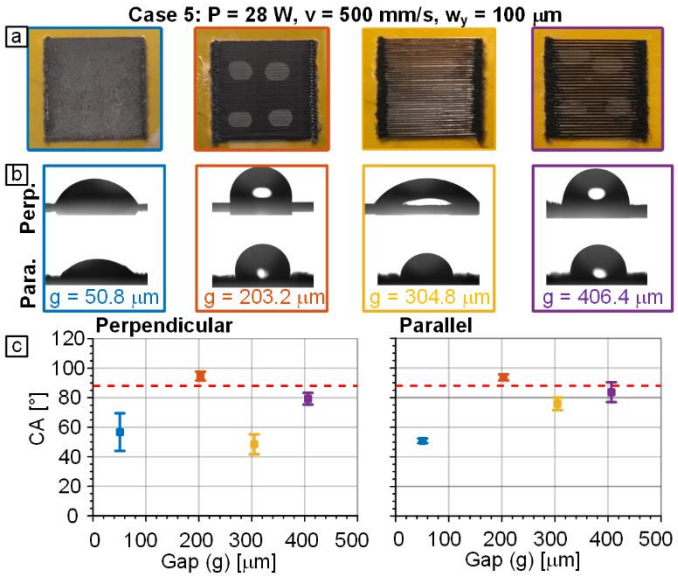

Figure 7: (a) Top view image of each patch for case 5 (lasing parameters P = 28W, v = 500 mm/s, w_y = 100 μm). (b) Optical tensiometer images of water droplets. (c) Plots of contact (CA) at different gap values. Red line represents control CA. Error bars represent ±standard deviation.

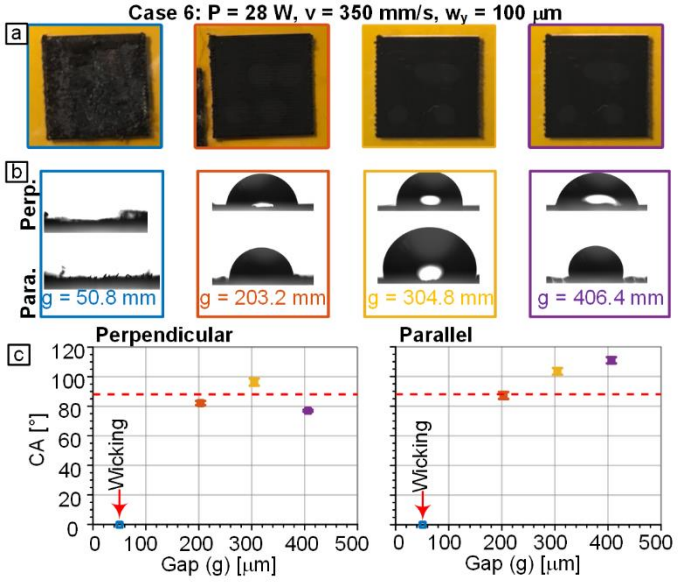

Figure 8: (a) Top view image of each patch for case 6 (lasing parameters P = 28W, v = 350 mm/s, w_y = 100 μm). (b) Optical tensiometer images of water droplets. (c) Plots of contact (CA) at different gap values. Red line represents control CA. Error bars represent ±standard deviation.

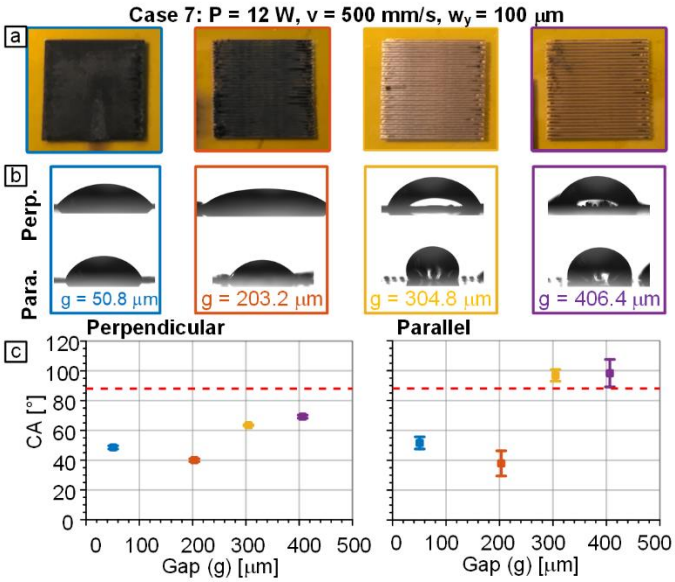

Figure 9: (a) Top view image of each patch for case 7 (lasing parameters P = 12W, v = 500 mm/s, w_y = 100 μm). (b) Optical tensiometer images of water droplets. (c) Plots of contact (CA) at different gap values. Red line represents control CA. Error bars represent ±standard deviation.

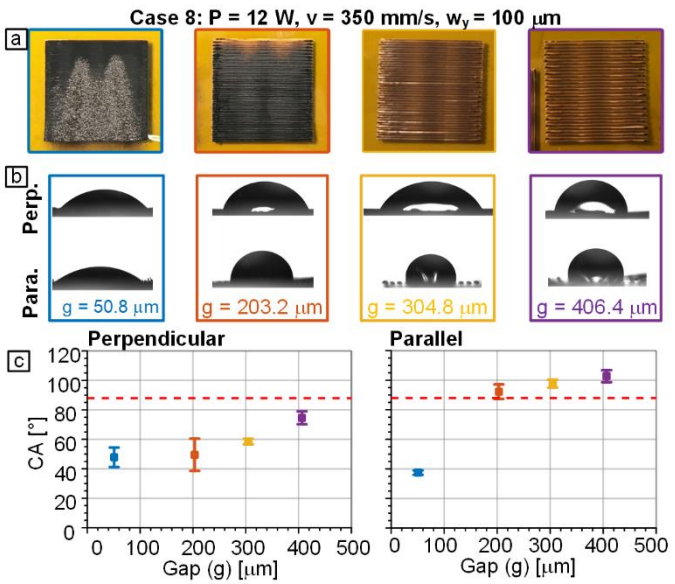

Figure 10: (a) Top view image of each patch for case 8 (lasing parameters P = 12W, v = 350 mm/s, w_y =100 μm). (b) Optical tensiometer images of water droplets. (c) Plots of contact (CA) at different gap values. Red line represents control CA. Error bars represent ±standard deviation.

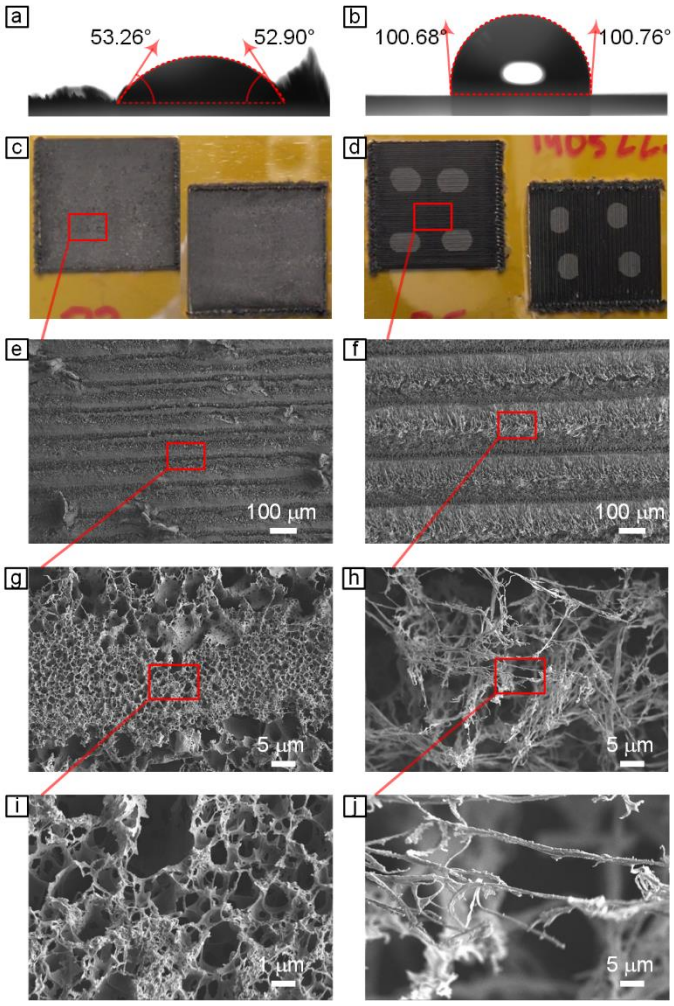

Figure 11: Contact angle measurements of power 28W, speed 500 mm/s, at (a) g = 50.8 µm, (b) g = 203.2 µm. (b-c) Top view Optical images of (a) and (b). (e, g, i) SEM images of (a) at 250x, 5,000x, and 25,000x, respectively. (f, h, j) SEM images of (b) at the same magnification.

SEM and optical imaging of two selected patches lased at identical power and lasing speed, but different gap sizes provides insight on the effect of line-to-line gap on morphology and contact angle. Optical images of the patch show that the patches have different colors and distinct macroscopic appearances that can be observed with the naked eye.

It was also observed that in some cases, a clear discoloration is observed where water droplets were located even after drying. For example the results shown in Figure 11 demonstrate this observation for the case of wider gap sample (Figure 11d), whereas in the small gap case (Figure 11c), no discoloration is observed. This indicates that capillary forces involved in water droplet drying significantly change the fibrous LINC morphology obtained at g = 203.2 µm. On the other hand, the connected nanoporous morphology at g = 50.8 µm are not significantly affected by capillary forces. Moreover, the anisotropic shape of these impressions confirm the anisotropic nature of the droplet contact on LINC lines.

In sum, we observe that some of the resulting contact angles are very low due to wicking effect of porous LINC morphology, while others exhibit decidedly hydrophobic contact angles due to the fibrous morphology. Also, some contact angles are highly anisotropic, owing to the effect of rastering gaps and water pinning on individual LINC lines. Hence, the approach shown in the paper provides a promising path to engineering anisotropic wetting behavior on commercial polymers. This capability has potential applications in the design of microfluidic devices, lab-on-a-chip sensors, microreactors, and self-cleaning surfaces.[13] This is a new approach to achieve anisotropic wetting surfaces[13]. Importantly, this approach is potentially more scalable and cost-effective compared to previously explored approaches. For example, anisotropic wetting was previously achieved using 1D topographical patterns created using expensive lithographical patterning [14], embossing [15], etching [16], as well as by creating areas of alternating surface energies [17]. Thus, using a direct-write commercial CO_2 laser processing system is a significant advantage of our approach.

5. CONCLUSIONS

We demonstrate that varying laser power, rastering speed, line-to-line gap, and spot size in laser induced nanocarbon (LINC) formation directly on polyimide surfaces enables tuning the contact angle of water. Our results show that a wide range of contact angles can be achieved, ranging from hydrophilic approaching 0° to hydrophobic surfaces approaching 120° as well as anisotropic wetting behavior. Characterizing the morphologies using a combination of optical and electron microscopy also enabled correlating these properties to the structure of LINC. Our findings highlight the versatility of this technique, which is promising for tuning the surface properties of commercial polymers for various applications, such as self-cleaning, anti-fouling, and self-cleaning surfaces.

ACKNOWLEDGMENTS

This research was supported partially by the National Science Foundation (Award Number: 1825772), and the Pitt Momentum seed grant from the University of Pittsburgh. Characterization was performed, in part, at the Nanoscale Fabrication and Characterization Facility, a laboratory of the Gertrude E. and John M. Petersen Institute of NanoScience and Engineering, housed at the University of Pittsburgh.

Table 2: Summary of results showing a color-coded classification of wetting behavior

Case	P(W)	v (mm/s)	w_y (µm)	g = 50.8 µm		g = 203.2 µm		g = 304.8 µm		g = 406.4 µm	
				⊥	∥	⊥	∥	⊥	∥	⊥	∥
1	28	500	300	22°	24°	83°	92°	95°	110°	24°	80°
2	28	350	300	95°	-	96°	101°	90°	99°	56°	93°
3	12	500	300	75°	81°	80°	80°	83°	89°	81°	95°
4	12	350	300	74°	82°	16°	29°	62°	81°	66°	88°
5	28	500	100	57°	51°	95°	94°	48°	76°	79°	84°
6	28	350	100	W	W	82°	87°	96°	104°	77°	111°
7	12	500	100	49°	52°	40°	38°	63°	97°	69°	98°
8	12	350	100	48°	38°	50°	92°	59°	98°	75°	103°

Hydrophilic <85 Hydrophobic >95 =85-95°

REFERENCES

[1] Lin, J., Peng, Z., Liu, Y., Ruiz-Zepeda, F., Ye, R., Samuel, E. L. G., Yacaman, M. J., Yakobson, B. I., and Tour, J. M., 2014, "Laser-Induced Porous Graphene Films from Commercial Polymers," Nat. Commun., **5**, pp. 1–8.

[2] Zhang, J., Zhang, C., Sha, J., Fei, H., Li, Y., and Tour, J. M., 2017, "Efficient Water-Splitting Electrodes Based on Laser-Induced Graphene," ACS Appl. Mater. Interfaces, **9**(32), pp. 26840–26847.

[3] Ye, R., Chyan, Y., Zhang, J., Li, Y., Han, X., Kittrell, C., and Tour, J. M., 2017, "Laser-Induced Graphene Formation on Wood," Adv. Mater., **29**(37), pp. 1–7.

[4] Li, Y., Luong, D. X., Zhang, J., Tarkunde, Y. R., Kittrell, C., Sargunaraj, F., Ji, Y., Arnusch, C. J., and Tour, J. M., 2017, "Laser-Induced Graphene in Controlled Atmospheres: From Superhydrophilic to Superhydrophobic Surfaces," Adv. Mater., **29**(27), pp. 1–8.

[5] Mamleyev, E. R., Heissler, S., Nefedov, A., Weidler, P. G., Nordin, N., Kudryashov, V. V., Länge, K., MacKinnon, N., and Sharma, S., 2019, "Laser-Induced Hierarchical Carbon Patterns on Polyimide Substrates for Flexible Urea Sensors," npj Flex. Electron., **3**(1), p. 2.

[6] Luo, S., Hoang, P. T., and Liu, T., 2016, "Direct Laser Writing for Creating Porous Graphitic Structures and Their Use for Flexible and Highly Sensitive Sensor and Sensor Arrays," Carbon N. Y., **96**, pp. 522–531.

[7] Duy, L. X., Peng, Z., Li, Y., Zhang, J., Ji, Y., and Tour, J. M., 2018, "Laser-Induced Graphene Fibers," Carbon N. Y., **126**(7), pp. 472–479.

[8] Singh, S. P., Li, Y., Zhang, J., Tour, J. M., and Arnusch, C. J., 2018, "Sulfur-Doped Laser-Induced Porous Graphene Derived from Polysulfone-Class Polymers and Membranes," ACS Nano, **12**(1), pp. 289–297.

[9] Luong, D. X., Yang, K., Yoon, J., Singh, S. P., Wang, T., Arnusch, C. J., and Tour, J. M., 2019, "Laser-Induced Graphene Composites as Multifunctional Surfaces," ACS Nano, **13**, p. acsnano.8b09626.

[10] Singh, S. P., Li, Y., Be'er, A., Oren, Y., Tour, J. M., and Arnusch, C. J., 2017, "Laser-Induced Graphene Layers and Electrodes Prevents Microbial Fouling and Exerts Antimicrobial Action," ACS Appl. Mater. Interfaces, **9**(21), pp. 18238–18247.

[11] Andrea, L., Francesco, P., Matteo, C., Mara, S., Marco, F., Stefano, B., Sergio, F., and Elena, T., 2017, "New Insights on Laser-Induced Graphene Electrodes for Flexible Supercapacitors: Tunable Morphology and Physical Properties," Nanotechnology, **28**(17), p. 174002.

[12] Vasile, E., Iordache, S. M., Ceaus, C., Stamatin, I., and Tiliakos, A., 2016, "Morphic Transitions of Nanocarbons via Laser Pyrolysis of Polyimide Films," J. Anal. Appl. Pyrolysis, **121**, pp. 275–286.

[13] Xia, D., Johnson, L. M., and Lõpez, G. P., 2012, "Anisotropic Wetting Surfaces with One-Dimesional

and Directional Structures: Fabrication Approaches, Wetting Properties and Potential Applications," Adv. Mater., **24**(10), pp. 1287–1302.

[14] Sommers, A. D., and Jacobi, A. M., 2006, "Creating Micro-Scale Surface Topology to Achieve Anisotropic Wettability on an Aluminum Surface," J. Micromechanics Microengineering, **16**(8), pp. 1571–1578.

[15] Liu, L., Jacobi, A. M., and Chvedov, D., 2009, "A Surface Embossing Technique to Create Micro-Grooves on an Aluminum Fin Stock for Drainage Enhancement," J. Micromechanics Microengineering, **19**(3).

[16] Wang, T., Li, X., Zhang, J., Wang, X., Zhang, X., Zhang, X., Zhu, D., Hao, Y., Ren, Z., and Yang, B., 2010, "Elliptical Silicon Arrays with Anisotropic Optical and Wetting Properties," Langmuir, **26**(16), pp. 13715–13721.

[17] Bliznyuk, O., Vereshchagina, E., Kooij, E. S., and Poelsema, B., 2009, "Scaling of Anisotropic Droplet Shapes on Chemically Stripe-Patterned Surfaces," Phys. Rev. E - Stat. Nonlinear, Soft Matter Phys., **79**(4), pp. 1–6.